A first principle study of the phase stability, ion transport and substitution strategy for highly ionic conductive sodium antipervoskite as solid electrolyte for sodium ion batteries

Ting Hei Wan[a], Ziheng Lu[a], Francesco Ciucci[a,b,*]

[a] Department of Mechanical and Aerospace Engineering, The Hong Kong University of Science and Technology, Hong Kong, China
[b] Department of Chemical and Biological Engineering, The Hong Kong University of Science and Technology, Hong Kong, China

HIGHLIGHTS

- Ab initio study on the promising solid electrolyte material Na_3OCl.
- Substituting alkali earth metal elements leads to increased Na migration barrier.
- Ca being identified as a potential candidate for substitution.

ARTICLE INFO

ABSTRACT

Materials in the Na-rich antiperovskite family are promising candidates as solid electrolytes (SEs) for all-solid-state Na-ion batteries (NIBs). In this work, we carry out *ab-initio* calculations to study various properties of Na_3OCl, namely the formation energies of various neutral defect pairs, the defect hopping barriers, the solution energies of high valence alkali earth metal substitutes to the Na atoms, and the effect of such substitution to the Na migration. While the introduction of alkali earth metal ions increases the Na vacancy concentration, the activation energy of Na transport also increases. Furthermore, we identify Ca as the most promising alkali earth metal to be doped into Na_3OCl due to its low binding energy and relatively small impact on the migration barrier. Our work provides a theoretical framework for further improving the Na conductivity of materials in the antiperovskite family for all-solid-state NIBs.

1. Introduction

The growing interest in renewable power sources has been accompanied by an increase in the demand for reliable energy storage systems. Although Li-ion batteries (LIBs) have been widely applied to electronic devices due to their high capacities and technological maturity, their prospects in large-scale grid-level storage of renewables are restricted by the limited availability of Li [1,2]. Because of the higher abundance of Na compared to Li [3], Na ion batteries (NIBs) have recently gained increasing attention [4–7]. It should be noted that safety is also an important issue for conventional LIBs and NIBs. To minimize the hazards, which include leakage of corrosive, toxic, and flammable organic liquid electrolytes, solid electrolytes (SEs) have been suggested as alternatives to traditionally used organic liquids [8–10].

In order to achieve reasonable performance, the SEs of the solid-state NIBs must possess an ionic conductivity of greater than 1 mS cm^{-1}, a negligible electronic conductivity, and a high chemical stability with respect to the applied voltage [11,12]. In light of this, β-alumina [8,13,14], which has an ionic conductivity of 2 mS cm^{-1} at room temperature [4], and $Na_{1+x}Zr_2Si_xP_{3-x}O_{12}$ (NASICON) based material [9,15,16], with ambient ionic conductivity as high as 3.5 mS cm^{-1}(for $Na_{3.1}Zr_{1.95}Mg_{0.05}Si_2PO_{12}$ [17]), have been widely investigated. Other popular materials within the research community include sulfide based Na conducting materials [18], such as the Na_3PS_4 glass [19,20]. Such materials are under intensive investigation due to their wide electrochemical window and electrode-electrolyte interface stability.

Nevertheless, the researches of novel Na-ion SEs are often inspired by materials that have been developed as Li SEs. This is not surprising as both Li and Na are in the alkali metal group. The alkali-metal-rich antiperovskite with chemical formula M_3OA (M= Li/Na, A= halogen) are among one of the most promising Li and Na SE materials [21]. The
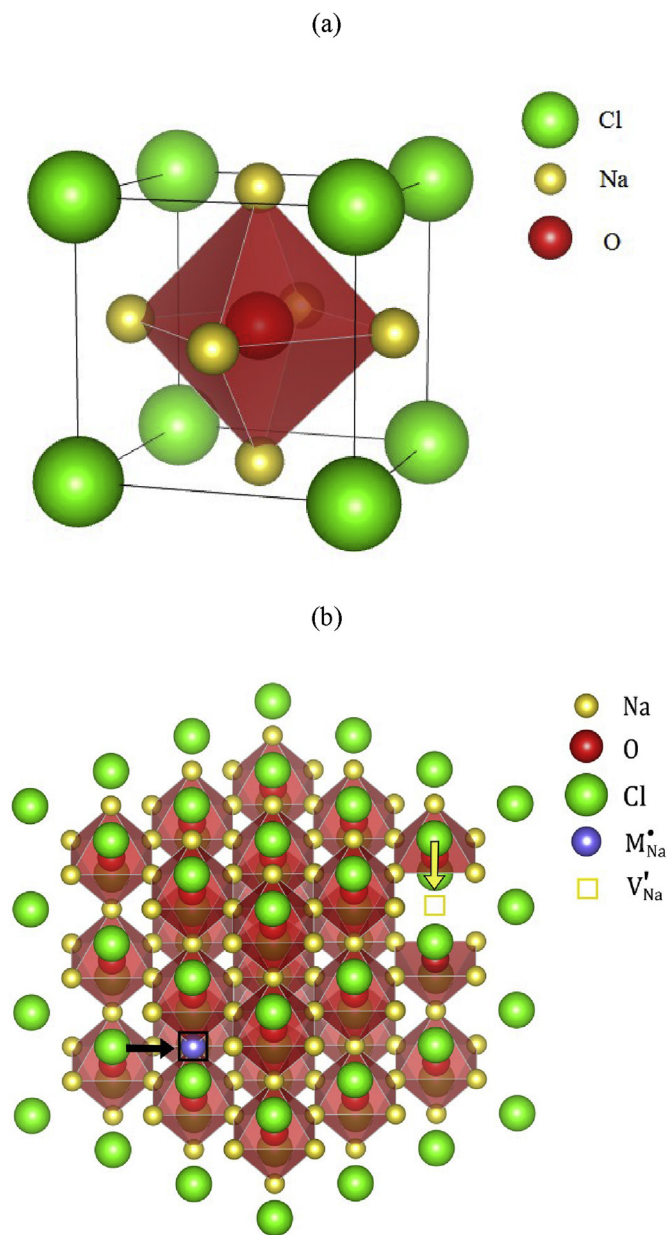
(a)

(b)

Fig. 1. (a) Atomic structure of Na_3OCl and (b) illustration of substituting alkaline earth metal into Na_3OCl. The purple sphere denotes the substitutional defect and yellow squared frame being V'_{Na} associated. (For interpretation of the references to colour in this figure legend, the reader is referred to the Web version of this article.)

prefix "anti" refers to the fact that the alkali metal cations occupy the O sites of typical perovskite oxides (*i.e.* ABO_3), while the halide and oxygen anion occupy the A site and B site, respectively. The structure of an anti-perovskite is shown in Fig. 1a.

Li-rich antiperovskite has shown excellent ionic conductivities as high as $1\,mS\,cm^{-1}$ at room temperature and $10\,mS\,cm^{-1}$ at $250\,^{\circ}C$ [21]. Although, the Na-rich antiperovskite has a lower ionic conductivity of $0.22\,mS\,cm^{-1}$ at $240\,^{\circ}C$ [22], researchers have improved the Na conductivity using elemental substitution. For example, Wang et al. [22] have shown that $Na_{2.9}Sr_{0.05}OBr_{0.6}I_{0.4}$ has an order of magnitude greater ionic conductivity compared to its un-modified counterpart, Na_3OBr, at $200\,^{\circ}C$. Moreover, the Goodenough group has recently reported that amorphous Na antiperovskites are superionic conductors with conductivity as high as $100\,mS\,cm^{-1}$ at around $150\,^{\circ}C$, far above the values obtained with other state-of-the-art SEs [23–25].

Due to the tremendous potential of Na-rich antiperovskites, compositional modification strategies for enhancing the ionic conductivity, *e.g.* the partial substitution of the Na site, are worth additional investigation. In this regard, we carried out an *ab-initio* study on the defect energy, substitutional energy, and Na transportation in Na_3OCl. We considered Na_3OCl because it is a prototypical antiperovskite, structurally analogous to the highly conductive Li_3OCl, and is less studied than Na_3OBr [26] and Na_4OI_2 [27]. In this work, we first investigated the defect formation energies of various plausible defects in Na_3OCl [28]. We considered three different types of neutral charged defect pairs: i) the Na Frenkel defect; ii) the NaCl Schottky defect pair; and iii) the Na_2O Schottky pair. For Na Frenkel defect pair, a lattice Na_{Na}^x ion is shifted to an interstitial site ($Na_i^{\bullet}$) leading to the formation of a Na vacancy V'_{Na} as follows:

$$Na_{Na}^x \rightleftharpoons V'_{Na} + Na_i^{\bullet} \tag{1}$$

The NaCl Schottky defect pair refers to the coexistence of a V'_{Na}, and a Cl vacancy, $V_{Cl}^{\bullet}$, formed by the following reaction:

$$Na_{Na}^x + Cl_{Cl}^x \rightleftharpoons V'_{Na} + V_{Cl}^{\bullet} + NaCl \tag{2}$$

The Na_2O Schottky pair corresponds to the formation of two V'_{Na}, and one O vacancy, $V_O^{\bullet\bullet}$, by the following reaction:

$$2Na_{Na}^x + O_O^x \rightleftharpoons 2V'_{Na} + V_O^{\bullet\bullet} + Na_2O \tag{3}$$
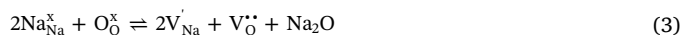
Our defect calculations suggest that NaCl Schottky defect pair is the energetically most stable among the three studied. This conclusion is similar to the one we have previously drawn for Li_3OCl [28]. The presence of V'_{Na} due to the NaCl Schottky defect pair suggests that the vacancy migration is the dominant diffusion mechanism. Since the diffusion of Na in the antiperovsike is likely mediated by V'_{Na}, an increase in the concentration of that defect may enhance the ionic conductivity. Hence, one strategy to improve the ionic conductivity of V'_{Na} is by partially substituting group II metal elements (*e.g.* Mg, Ca, Sr and Ba) into the Na site resulting in the creation of a $M_{Na}^{\bullet}$ defect. In turn, this leads to the formation of V'_{Na} by charge compensation. Consequently, we studied the impact of such substitution on the conductivity and we calculated the substitutional energies, *i.e.,* the energy necessary to form $M_{Na}^{\bullet} - V'_{Na}$ defect pairs via the following reaction:

$$2Na_{Na}^x + MO \rightarrow V'_{Na} + M_{Na}^{\bullet} + Na_2O \tag{4}$$
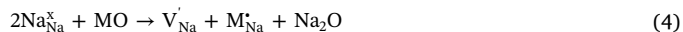
We also calculated the $M_{Na}^{\bullet} - V'_{Na}$ binding energy corresponding to the energy required for a V'_{Na} to detach from the attraction of a neighboring $M_{Na}^{\bullet}$. We then studied the impact of the substitution on the Na migration by both nudged elastic band (NEB) and *ab-initio* molecular dynamics (AIMD) simulations. Our results illustrate that although $M_{Na}^{\bullet}$ substitution effectively increases V'_{Na} concentration in Na_3OCl, the $M_{Na}^{\bullet} - V'_{Na}$ attraction leads to an increased activation energy for the migration of Na. This results in a lower conductivity given an identical V'_{Na} concentration. One can select a $M_{Na}^{\bullet}$ substitutional defect with weaker $M_{Na}^{\bullet} - V'_{Na}$ attraction to minimize the increase in migration barrier. Because of a relatively smaller binding energy and, hence, a weaker $Ca_{Na}^{\bullet} - V'_{Na}$ attraction, we propose that Ca is a potential candidate for substitution of Na_3OCl.

2. Computational methods

In this study, the density functional theory (DFT) simulations were carried out using the VASP code [29]. The projector augmented wave (PAW) method was used with the Perdew–Burke–Ernzerhof generalized gradient approximation [30]. The defect formation and substitutional energies were calculated by the structural relaxation of the initial lattice. These relaxations were carried out on $3 \times 3 \times 3$ supercell with 135 atoms. A $3 \times 3 \times 3$ Monknorst-Pack grid was used to sample the Brillouin zone [31]. For the three elements of the original material, *i.e.,* Na, O and Cl, we used pseudopotentials with $2p^63s^1$, $2s^22p^4$, and $2s^22p^5$
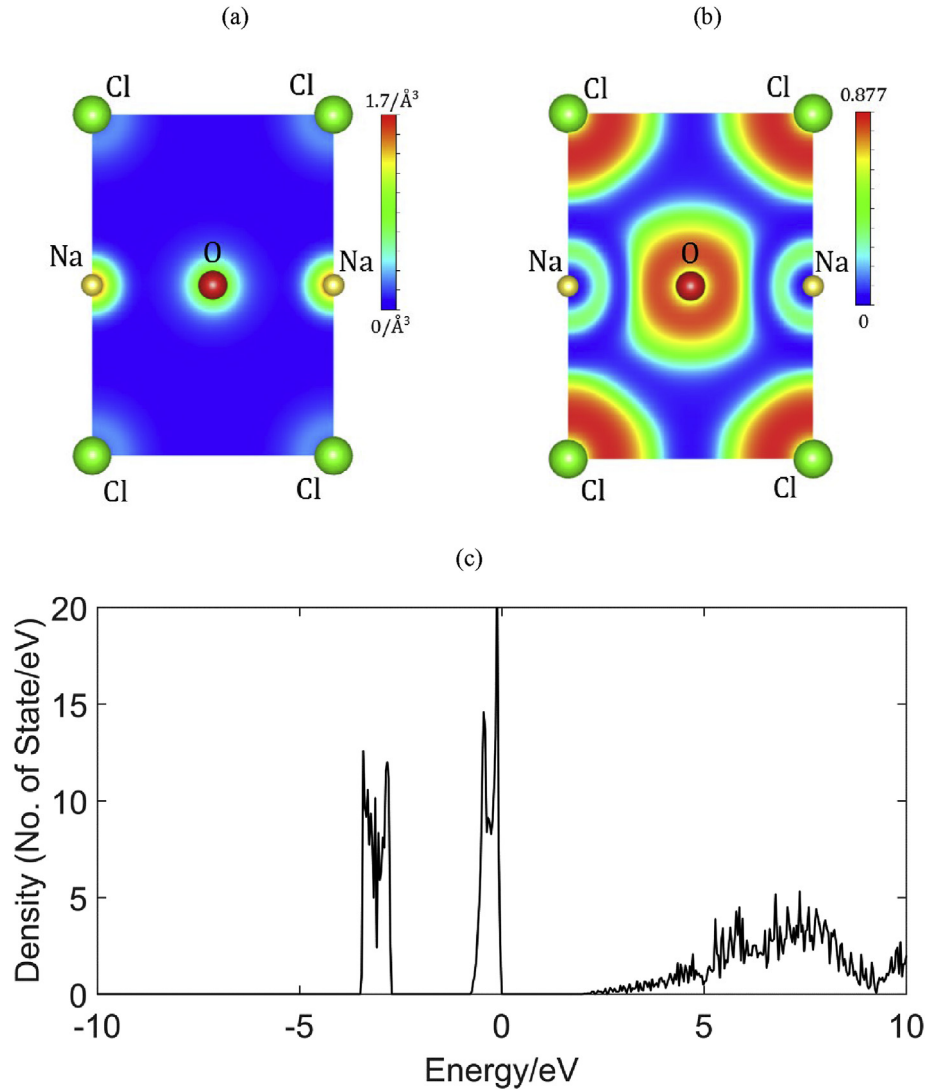
(a)   (b)

(c)

Fig. 2. (a) Valence electron density of Na_3OCl at the (110) plane. (b) ELF of the Na_3OCl at the (110) plane. (c) The electron density of state of Na_3OCl.

Table 1
Defect energies for various configurations and defect types. Bolded numbers indicate the lowest energies for each type of defect.

Na Frenkel defect pair ($Na_{Na}^x \rightarrow V'_{Na} + Na_i^{\bullet}$)			
Configuration	NN	2NN	3NN
Energies (eV)	**1.57**	1.93	1.94

NaCl Schottky defect pair ($Na_{Na}^x + Cl_{Cl}^x \rightarrow V'_{Na} + V_{Cl}^{\bullet}+NaCl$)			
Configuration	NN	2NN	3NN
Energies (eV)	1.24	**1.18**	1.28

Na_2O Schottky defect pair ($2Na_{Na}^x + O_O^x \rightarrow 2V'_{Na} + V_O^{\bullet\bullet} + Na_2O$)			
Configuration	Adjacent	Opposite	Separated
Energies (eV)	**1.74**	1.88	2.52

valence configuration, respectively. As for the pseudopotentials of the Mg, Ca, Sr, and Ba we investigated for substitution, we considered the $2s^2 2p^6 3s^2$, $3s^2 3p^6 4s^2$, $4s^2 4p^6 5s^2$, and $5s^2 5p^6 6s^2$ valence configuration, respectively. The energy cutoff was set at 600 eV. For all structural relaxations, the conjugate gradient algorithm was used for minimizing the energy with a convergence criterion set at 10^{-5} eV.

In addition to the defect formation energy and substitutional energy calculations, we also conducted NEB computations to study the effect of substitutional defects on the Na migration energy. Every NEB calculation was carried out with a $3 \times 3 \times 3$ supercell a force convergence of 0.05eV/Å. 3 images were considered for both the NEB calculations with and without substitutional defects. To elucidate the Na ion transport mechanism and estimate the activation enthalpy, we performed AIMD simulations using an NVT ensemble with a Nosé thermostat [32]. For the pristine Na_3OCl, the simulations were done in a $2 \times 2 \times 2$ supercell with one Na ion being removed from each supercell to create a vacancy necessary for the Na ion transport. As for the doped system, the V'_{Na} directly generated by the substitution allows the Na ion hopping within the supercell and no additional Na ion removal is needed. For each AIMD simulation, the computation time length was set at 100 ps and the time step at 2 fs. The AIMD simulations were performed at elevated temperatures (between 800 K and 1500 K) for the calculation of the activation energies. Although the simulated temperatures are much higher than the melting temperature of pristine Na_3OCl (~550 K) [22], the NVT ensemble used excludes the thermal expansion of the lattice and, thereby, prevents melting in the considered temperature range. Moreover, such high simulation temperatures are chosen to allow for sufficient number of Na hopping events. This choice ultimately improves the accuracy of the calculated self-diffusion coefficient and the correspondingly estimated ionic conductivities [33,34].
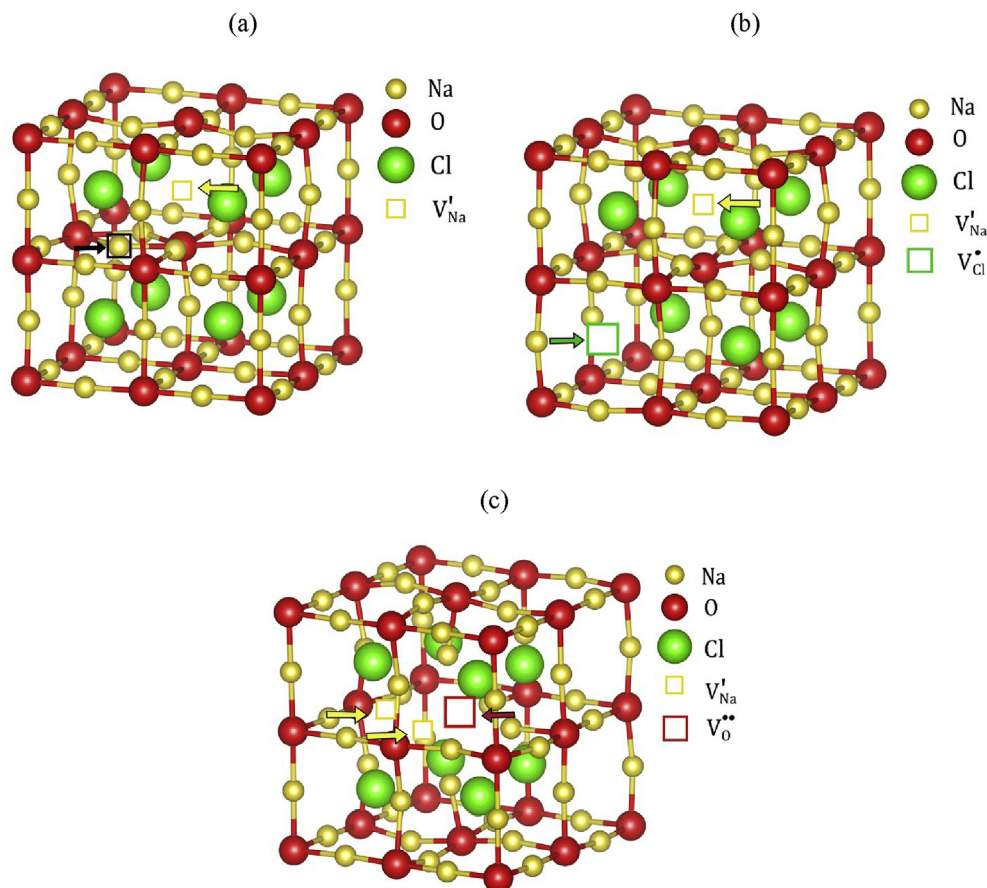
(a)

(b)

(c)

Fig. 3. The lowest energy configuration for (a) Na Frenkel defect pair (NN), (b) NaCl Schottky defect pair (2NN), and (c) Na_2O Schottky defect pair (adjacent). The yellow, green and red squares denote V'_{Na}, $V^{\bullet}_{Cl}$, and $V^{\bullet\bullet}_{O}$. The black square frames indicate the interstitial defect $Na^{\bullet}_i$. (For the sake of illustration, $2 \times 2 \times 2$ supercell is shown instead of the $3 \times 3 \times 3$ supercell). (For interpretation of the references to colour in this figure legend, the reader is referred to the Web version of this article.)

3. Results and discussion

3.1. Lattice structure, electronic property, and phase stability of Na_3OCl

We first studied the lattice structure, the electronic properties and phase stability of the Na_3OCl by relaxing the defect-free supercell. The optimization leads to a cubic antiperovskite structure with a unit cell lattice parameter of 4.54 Å in agreement with both experimental [35] and simulation [36] reports. The nature of the atomic bonding inside the lattice was studied thanks to the electron localization function (ELF) analysis [37]. As shown in Fig. 2a, the valence electrons tend to localize around the nucleus of the bonded atoms. Also, in Fig. 2b, small ELF magnitude regions are observed in between the atomic lattice points. Both computations indicate that, in agreement with intuition, the bonds in Na_3OCl are ionic. The ionic nature of the antiperovskite suggests that the material is electrically non-conductive. Also, we calculated the density of state (DOS) of electrons as shown in Fig. 2c. The resulting DOS suggest a band gap of around 2.0 eV, and that the antiperovskite can act as the solid-state electrolyte for small voltage NIBs.

It is also critical that the SE is chemically stable. Such stability can be qualitatively assessed by considering the formation energy of the material [38]. Wang et al. [22] has reported that Na_3OCl can be synthesized by sintering Na_2O and NaCl powders through the following chemical reaction:

$$Na_2O + NaCl \rightarrow Na_3OCl \tag{5}$$

The calculated formation energy of Na_3OCl is $E_{formation} = E_{Na_3OCl} - E_{Na_2O} - E_{NaCl} = 72.7$ meV/formula unit, a value that suggest that Na_3OCl is likely to be metastable and can be stabilized by pressure

or entropy at room temperature [22]. A similarly low and positive formation energy of 69.5 meV/formula unit was also found for Li_3OCl [38]. This suggests that both Na_3OCl and its lithium-rich counterpart have similar thermodynamic characteristics. Nonetheless, one should note that the formation energy computed above is only a proxy for the chemical stability of the bulk material. It is known that, in solid-state batteries, decomposition reactions may take place at the electrode-electrolyte interface, leading to the formation of interlayer. One can investigate such interfacial chemical instability by taking into account the reaction enthalpy between a specific electrode and Na_3OCl [39].

3.2. Neutral defect pairs formation energy

Two mechanisms, one mediated by vacancies and another by interstitials, have been proposed for the ionic transportation in the antiperovskite family [40]. Since the ionic migration is achieved by the presence of suitable carriers, *i.e.*, intrinsic defects existing inside the lattice, one should first identify whether charge carriers are likely to be generated by studying the defect formation energies. In this regard, we closely followed the strategy of our previous work [28] and considered the defect energies of three charge neutral defect pairs, *i.e.*, the Na Frenkel defect pair, the NaCl Schottky defect pair, and the Na_2O Schottky defect pair, where the corresponding formation reactions are given in (1)–(3). We choose these three types of defect because they are commonly investigated [28,41].

To obtain the lowest energy configuration, we examined the three configurations with the lowest energies for each type of defect pair. The configurations investigated for the three types of defect pair are shown in Figure S1–S3 of the Supplementary Information. The calculated
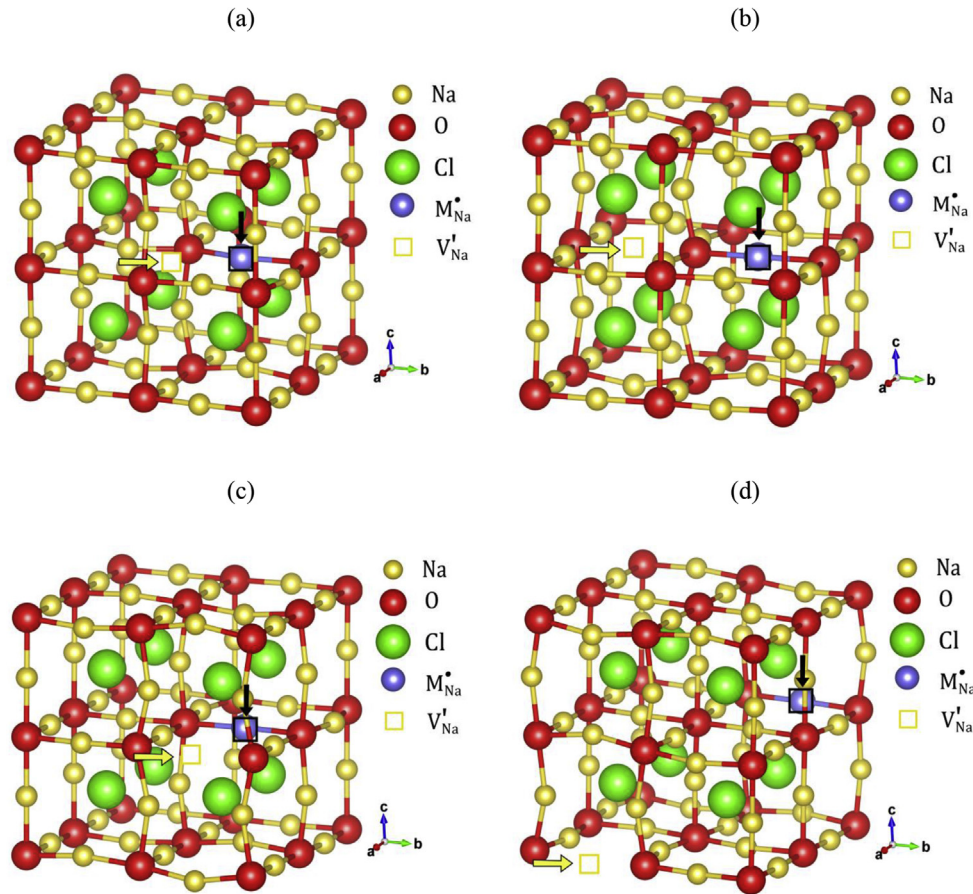
(a)   (b)

(c)   (d)

Fig. 4. Possible configuration of substitutional defect and vacancy pairs (V_{Na}', $M_{Na}^{\bullet}$). Purple spheres represent $M_{Na}^{\bullet}$ and yellow squares represent the V_{Na}' associated. Panel (a)–(d) shows the adjacent, opposite 1, opposite 2 and separated $M_{Na}^{\bullet} - V_{Na}'$ configuration respectively. For the sake of illustration, the $2 \times 2 \times 2$ supercell is shown *in lieu* of the $3 \times 3 \times 3$ supercell used in the computations. (For interpretation of the references to colour in this figure legend, the reader is referred to the Web version of this article.)

Table 2
The lattice energies of various oxides used for calculating the solution energy.

Oxides	Lattice Energy (eV/f.u.)
Na$_2$O	−11.3
MgO	−12.0
CaO	−12.9
SrO	−12.1
BaO	−11.6

Table 3
The computed solution and binding energies of various alkaline earth metal oxides into Na$_3$OCl. The bolded values are the energy of the most favorable $M_{Na}^{\bullet} - V_{Na}'$ configuration for each alkaline earth metal oxide.

Solution Energy (eV/unit substitutional defect)				
Substitutional Defects	Mg$_{Na}^{\bullet}$	Ca$_{Na}^{\bullet}$	Sr$_{Na}^{\bullet}$	Ba$_{Na}^{\bullet}$
Adjacent	2.01	1.61	**1.28**	**0.773**
Opposite 1	**1.93**	**1.56**	1.35	1.06
Opposite 2	2.21	1.82	1.61	1.23
Separated	2.18	1.67	1.44	1.19
Binding Energy (eV/substitutional defect-vacancy pair)				
Energy per (V_{Na}', $M_{Na}^{\bullet}$) pair	0.246	0.104	0.152	0.419

defect energies of each defect pair on each of the considered configurations are shown in Table 1. For Na Frenkel defect pair, the lowest energy configurations for Na Frenkel defect pair is the nearest neighbor configuration (NN), as shown in Fig. 3a, where Na$_i^{\bullet}$ and V_{Na}' are the closest together without further relaxation to the non-defected state. The lowest energy configurations for NaCl Schottky, and Na$_2$O Schottky defect pair are the second nearest neighbor (2NN), and adjacent configuration respectively, as shown in Fig. 3b and c. The results are in agreement with our previous work on Li$_3$OCl [28].

Among the three neutral defect pairs studied, the NaCl Schottky defect pair has the lowest formation energy. This conclusion is analogous to the one we previously obtained for Li$_3$OCl [41]. Furthermore, it indicates that Na vacancy hopping is the likely Na transport mechanism in Na$_3$OCl. Nonetheless, we need to point out that our calculations may only be valid for Na$_3$OCl and may not necessarily apply to other Na-rich antiperovskites (*e.g.* Na$_3$OBr). In fact, Zhu et al. have found from in-situ neutron diffusion that the dominant neutral defect type is Na$_2$O Schottky defect pair for Na$_3$OBr [27]. One should perform similar defect energies calculations for other Na-rich antiperovskites to identify their dominating neutral defect type accordingly.

3.3. Substitutional defects: solution and binding energies

Substituting a divalent metal in the Na site ($M_{Na}^{\bullet}$) leads to the formation of an extra V_{Na}' in the lattice, as illustrated by (4). This may, in turn, enhance the ionic conductivity of the material. To explore which

Table 4
The charge of the substitutional defect as calculated from Bader charge analysis. The bolded values correspond to the Bader charge of the lowest energy $M_{Na}^{\bullet} - V_{Na}^{'}$ configuration.

Bader Charge				
	$Mg_{Na}^{\bullet}$	$Ca_{Na}^{\bullet}$	$Sr_{Na}^{\bullet}$	$Ba_{Na}^{\bullet}$
Adjacent	+1.65	+1.46	**+1.49**	**+1.43**
Opposite 1	**+1.64**	**+1.46**	+1.47	+1.52

metal oxide MO, we calculated $E_{solution}$ the energy of the reaction (4), or the solution energy, by Ref. [42]

$$E_{solution} = E_{M_{Na}^{\bullet} - V_{Na}^{'}} + E_{Na_2O} - E_{Na_{Na}^{x}} - E_{MO} \qquad (6)$$

where $E_{M_{Na}^{\bullet} - V_{Na}^{'}}$ is the lattice energy of the doped material with the corresponding $V_{Na}^{'}$ defect, $E_{Na_{Na}^{x}}$ is the lattice energy of the pristine structure, E_{Na_2O} and E_{MO} are the energies of Na_2O and MO, respectively. The solution energies of the various oxides used for our calculations are reported in Table 2.

The calculated solution energies of various substitutional defects and configurations are shown in Table 3. The solution energy can be regarded as an indicator of the stability of the material upon substitution. Smaller solution energy may imply that substitution is easier. For all the cases studied, we have $E_{solution} > 0$, which implies that substituting alkaline earth elements into the Na site likely destabilizes the antiperovskite structure. Intuitively, this can be attributed to the ionic size mismatch of $M_{Na}^{\bullet}$ and associated $V_{Na}^{'}$ relative to the original Na cations. Such size difference induces an internal strain around the substitutional defect and destabilizes the lattice [43]. In addition, the results indicate that the $E_{solution}$ decreases with the increasing size of $M_{Na}^{\bullet}$. Our calculations suggest that Ba is the most stable substitutional defect among the ones studied. For smaller alkaline earth metal, *i.e.*, $Mg_{Na}^{\bullet}$ and $Ca_{Na}^{\bullet}$, the opposite 1 $M_{Na}^{\bullet} - V_{Na}^{'}$ configuration results in slightly smaller solution energies. Instead for the larger $Sr_{Na}^{\bullet}$ and $Ba_{Na}^{\bullet}$, the adjacent configuration has the lowest energy. Nonetheless, we notice that for $Mg_{Na}^{\bullet}$, $Ca_{Na}^{\bullet}$ and $Sr_{Na}^{\bullet}$, the solution energy difference between the second lowest and the lowest energy configuration are around 3–5% with respect to the lowest energy configuration. This implies that the adjacent and opposite 1 configurations may be equally probable in the practical thermodynamic environment. On the other hand, for $Ba_{Na}^{\bullet}$, the energy of the opposite 1 configuration is about 37% higher compared to the adjacent configuration. This indicates that $V_{Na}^{'}$ associated with $Ba_{Na}^{\bullet}$ has a high tendency to stay in the adjacent configuration probably because of the large lattice distortions originating from Ba's large ionic radius. A compact $Ba_{Na}^{\bullet} - V_{Na}^{'}$ configuration is more favorable because it limits the distortion imposed to the lattice.

In addition to the solution energy, we also need to determine whether the $V_{Na}^{'}$ is tightly bound to its counterpart in the substitutional defect pair. Therefore, we calculated the binding energies of $M_{Na}^{\bullet}$ with $V_{Na}^{'}$ based on the following formula [44]

$$E_{binding} = \left(E_{M_{Na}^{\bullet}} + E_{V_{Na}^{'}} \right) - \left(\min\left(E_{M_{Na}^{\bullet} - V_{Na}^{'}} \right) + E_{Na_{Na}^{x}} \right) \qquad (7)$$

where $E_{M_{Na}^{\bullet}}$ and $E_{V_{Na}^{'}}$ are the energies when a lattice Na_{Na}^{x} is replaced by a substitutional ion and a $V_{Na}^{'}$, respectively, and $\min\left(E_{M_{Na}^{\bullet} - V_{Na}^{'}} \right)$ refers to the lattice energy of the most favorable $M_{Na}^{\bullet} - V_{Na}^{'}$ configuration as identified by the above solution energy calculations. The $E_{binding}$ is smallest when Ca is substituted into the lattice, see Table 3. Since the lattice with substitutional defect remains ionic in nature, the binding energies of the $M_{Na}^{\bullet} - V_{Na}^{'}$ pairs largely depend on the coulombic attraction. In turn, the coulombic interaction is a result of the $M_{Na}^{\bullet} - V_{Na}^{'}$ distance and the $M_{Na}^{\bullet}$'s effective charge, which can be determined by the Bader charge analysis [45]. As shown in Table 4, a smaller ionic radius of $M_{Na}^{\bullet}$ correlates with the larger Bader charge at its most favorable $M_{Na}^{\bullet} - V_{Na}^{'}$ configuration. On the other hand, the adjacent configuration is more energetically favorable for larger substitutional defects, *i.e.*, Sr and Ba. The $M_{Na}^{\bullet} - V_{Na}^{'}$ distance is smaller for the adjacent case than the opposite 1 configuration, which corresponds to stronger coulombic attraction between $M_{Na}^{\bullet}$ and $V_{Na}^{'}$. $Ca_{Na}^{\bullet}$ has smaller effective charge than $Mg_{Na}^{\bullet}$ due to the shielding effect of its extra electron shell. Meanwhile, the opposite 1 configuration results in a longer $Ca_{Na}^{\bullet} - V_{Na}^{'}$ distance than then $Sr_{Na}^{\bullet} - V_{Na}^{'}$ pair. The combined effect of a smaller effective charge of $Ca_{Na}^{\bullet}$ and longer $Ca_{Na}^{\bullet} - V_{Na}^{'}$ distance leads to weaker $Ca_{Na}^{\bullet} - V_{Na}^{'}$ binding, and hence, the smallest $E_{binding}$ among the $M_{Na}^{\bullet} - V_{Na}^{'}$ pairs studied.
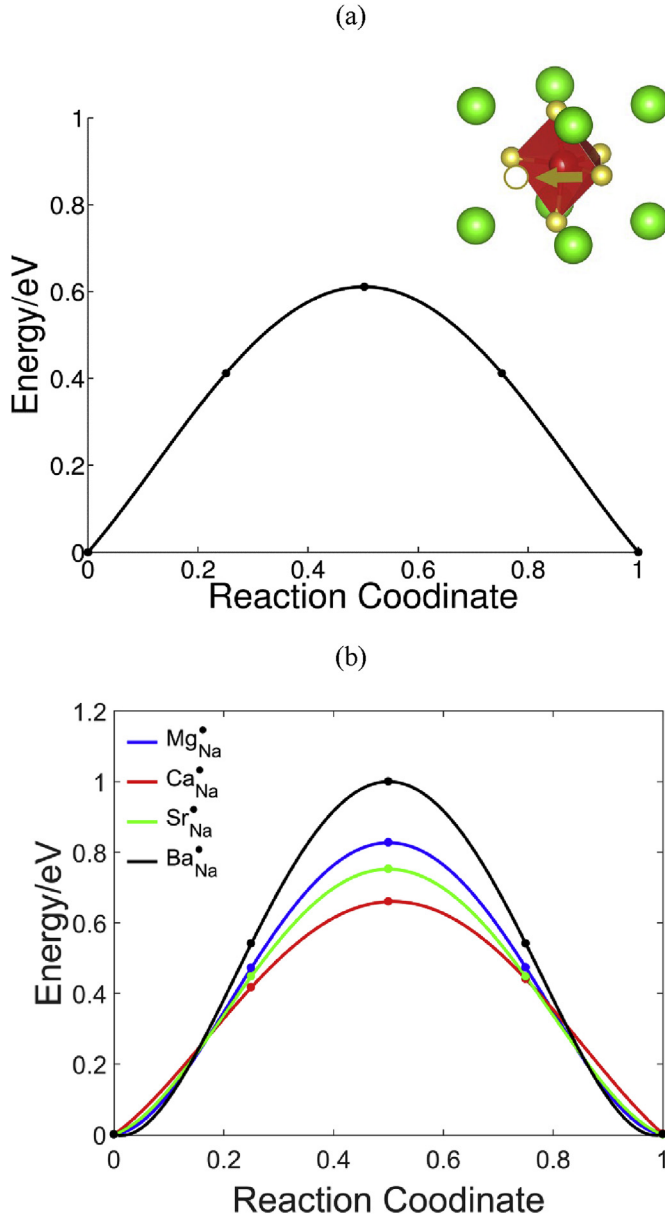
(a)

(b)

Fig. 5. (a) The energy-reaction coordinate plot for $V_{Na}^{'}$ hopping in pristine Na_3OCl. The inset illustrates the $V_{Na}^{'}$ migration path. (b) The reaction coordinate plot as obtained from NEB calculation of path 1 of the doped system.

alkaline earth metal element (*i.e.* Mg, Ca, Sr, and Ba) increases the conductivity the most, we calculated both the solution and binding energies for Na_3OCl substituted with the alkaline earth metal elements. In particular, we considered four unique $M_{Na}^{\bullet} - V_{Na}^{'}$ configurations, *i.e.*, adjacent, opposite 1, opposite 2, and separated configuration, as illustrated in Fig. 4. For each $M_{Na}^{\bullet} - V_{Na}^{'}$ configuration and alkaline earth

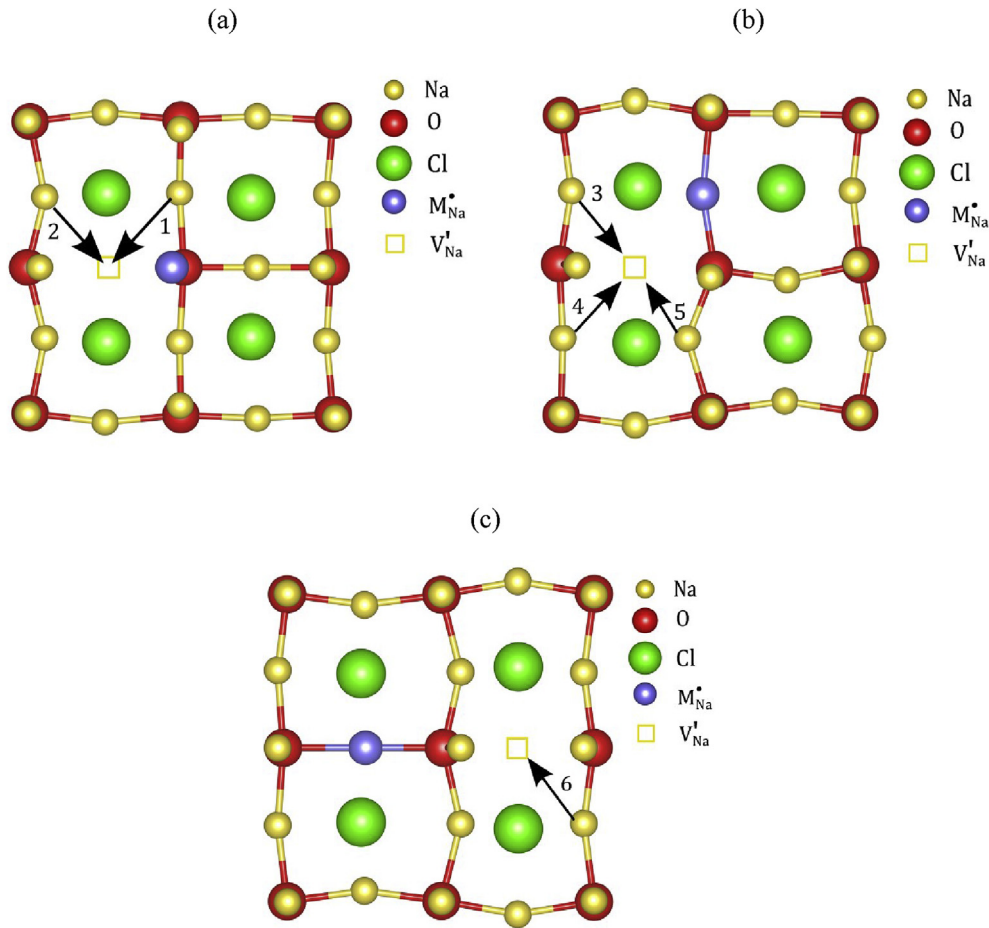(a)   (b)

(c)

Fig. 6. Illustration of the migration path of V'_{Na} being considered when substitutional defect is being added. Panel (a) shows the a-b plane cross section of the adjacent configuration. Panel (b) shows the a-c plane cross section of the adjacent $V'_{Na} - M^{\bullet}_{Na}$ configuration. Panel (c) shows the a-c plane cross section of the opposite 1 $V'_{Na} - M^{\bullet}_{Na}$ configuration.

Table 5
The NEB barrier encountered by a migrating Na ion. The bolded values indicate the minimum value across each path.

Migration Energy Barrier(eV)

Path	$Mg^{\bullet}_{Na}$	$Ca^{\bullet}_{Na}$	$Sr^{\bullet}_{Na}$	$Ba^{\bullet}_{Na}$
1	0.827	**0.661**	0.752	1.00
2	0.714	**0.682**	0.787	0.968
3	**0.722**	0.761	0.847	1.19
4	0.732	**0.705**	0.767	0.719
5	**0.635**	0.676	0.647	0.779
6	0.753	0.760	0.710	**0.583**

3.4. Sodium transport

3.4.1. Vacancy mediated sodium migration

The defect energy study in section 3.2 confirmed the reports in literature that Na migration in Na$_3$OCl occurs via a vacancy hopping mechanism by which a lattice Na ion diffuses by jumping to a nearby vacant site [22,27]. Here we calculate the energy barrier of this hop (this is also known as migration energy) by NEB simulations. The energy-reaction coordinate for the Na diffusion is plotted in Fig. 5a, indicating a migration barrier of 0.61eV. The inset of Fig. 5a illustrates the path for the vacancy-mediated mechanism as predicted by the NEB simulation. Although the addition of $M^{\bullet}_{Na}$ boosts the vacancy concentration in the lattice, the associated V'_{Na} need to migrate away from the local minimum near the $M^{\bullet}_{Na}$. Therefore, we conducted NEB

simulations also for the doped case. We identified six unique diffusion paths around the two lowest energy $M^{\bullet}_{Na} - V'_{Na}$ configurations, *i.e.*, the adjacent and opposite 1 configuration. The six diffusion paths are illustrated in Fig. 6. Here, path 1 refers to the transition from adjacent to another adjacent $M^{\bullet}_{Na} - V'_{Na}$ configuration. Path 2 and 3 correspond to the transition from adjacent to opposite 1 and from adjacent to the opposite 2 configurations respectively. The NEB simulation results for various defect interacted Na migration via path 1 is presented in the energy-reaction coordinate plots in Fig. 5b. The energy-reaction plots for other paths considered are included in Fig. S4 of the Supplementary Information. The migration energy barriers of different substitutional defects and paths are shown in Table 5.[1]

For all paths studied, the presence of the $M^{\bullet}_{Na}$ leads to an increase of the Na migration barrier compared to the defect-free case. We also noted that the migration energy barrier depends on the substitutional energy of the respective $M^{\bullet}_{Na} - V'_{Na}$ configuration. As discussed in section 3.3, an V'_{Na} associated to $Mg^{\bullet}_{Na}$ and $Ca^{\bullet}_{Na}$ has a lower energy in the opposite 1 configuration compared to the adjacent configuration. Therefore, the energies required for V'_{Na} to migrate from the opposite 1 $M^{\bullet}_{Na} - V'_{Na}$ configuration to the Na site that is further away from the substitutional defect (*i.e.* path 6) are higher for $Mg^{\bullet}_{Na}$ and $Ca^{\bullet}_{Na}$ substitution. Conversely, the migration energy barriers of paths 1–5 are

---

[1] There are some situations where the V'_{Na} moves from a higher energy $M^{\bullet}_{Na} - V'_{Na}$ configuration to the lower energy configuration (*e.g.* Path 2 of $Mg^{\bullet}_{Na}$ substitution). To allow reasonable comparison between different substitutional defects, the values we tabulated in Table 5 are the highest migration barrier among the forward and backward migration for each path.
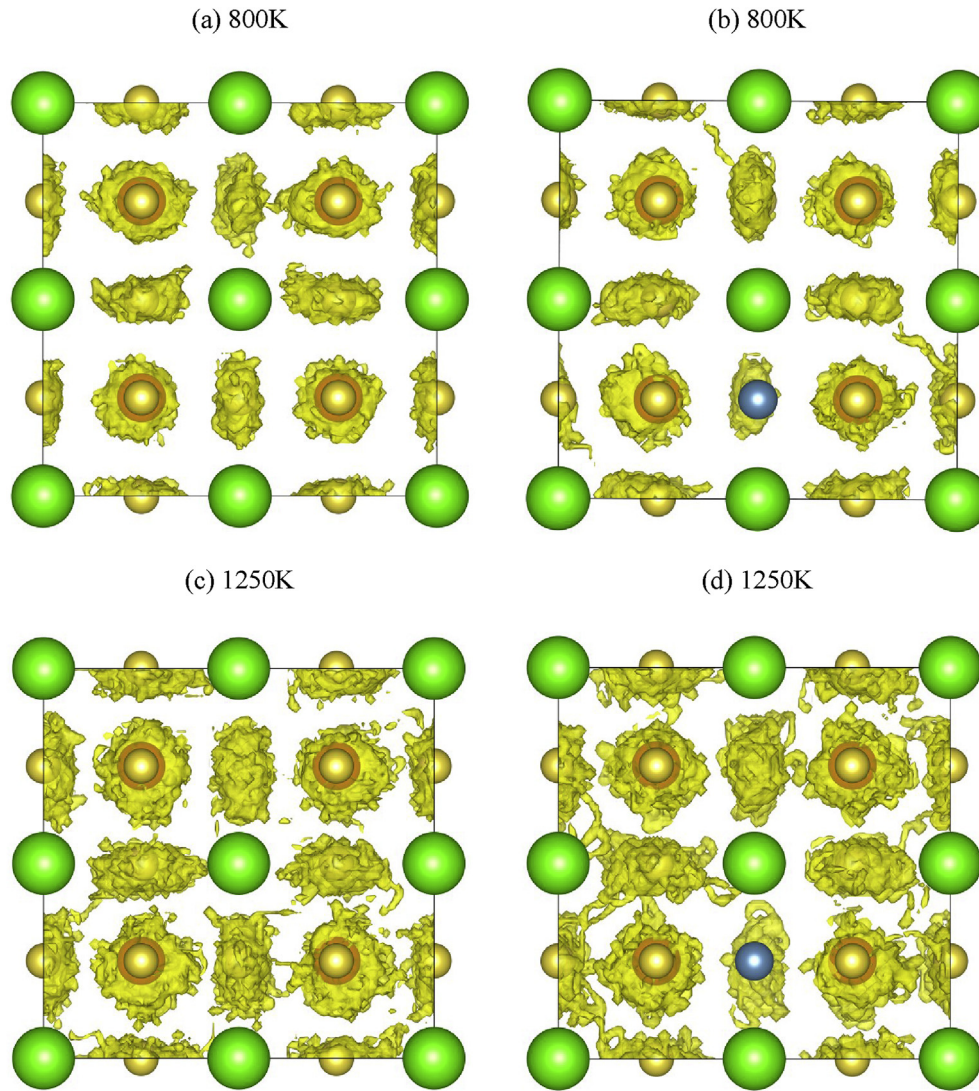
(a) 800K (b) 800K

(c) 1250K (d) 1250K

Fig. 7. The Na nuclear density plot of the Na$_{2.875}$OCl, panel (a) and (c), and Na$_{2.75}$Ca$_{0.125}$OCl, panel (b) and (d), as computed from AIMD at 800 K and 1250 K. Yellow, red, green and blue spheres are the Na, O, Cl, and Ca ions respectively. (For interpretation of the references to colour in this figure legend, the reader is referred to the Web version of this article.)

higher for Sr$^{\bullet}_{Na}$ and Ba$^{\bullet}_{Na}$ substitution since their adjacent M$^{\bullet}_{Na}$ − V$^{'}_{Na}$ configuration has the lowest energy compared to the other configurations.

3.4.2. Transport pathway from ab-initio molecular dynamics simulation

To validate the Na ion transport mechanism and further confirm the impact of the substitutional defect on Na diffusion, we conducted AIMD in both the pristine and the doped system. Since Ca$^{\bullet}_{Na}$ leads to the lowest Ca$^{\bullet}_{Na}$ − V$^{'}_{Na}$ binding energy and the lowest migration barrier among all the substitutional defects considered, we only investigated the effect of Ca$^{\bullet}_{Na}$ substitution for our AIMD simulation. As shown in Fig. S5 the mean square displacement plot for both Na$_{2.875}$OCl, and Na$_{2.75}$Ca$_{0.125}$OCl, only Na ion have a significant mean-squared displacement at 1500 K. The other atoms just oscillate about their starting positions. In spite of the high temperature, no melting is observed because the AIMD computation is constrained to be in the NVT ensemble [38]. Fig. 7 shows the Na ion trajectories for the Na$_{2.875}$OCl, and Na$_{2.75}$Ca$_{0.125}$OCl at 800 K and 1250 K. At the temperatures considered, only the Na ions hop to the adjacent vacant sites. The overlapping between adjacent Na nuclear density clusters increases with temperature indicating the formation of a Na transportation pathway.

Moreover, the result of AIMD allows us to estimate the Na ion conductivity, σ, and the activation energy, E$_a$, of the Na diffusion in the material. The relationship between these two quantities is given by the Arrhenius relation, *i.e.*, σ T$\propto$ exp(−E$_a$/k$_B$T), where T is the temperature. We estimated the activation energy by computing the slope of log(σT) versus the inverse of temperature. Fig. 8 shows the Arrhenius plot for the AIMD result. At the simulation temperatures considered, the conductivity of Na$_{2.875}$OCl and Na$_{2.75}$Ca$_{0.125}$OCl are comparable, as shown in Fig. 8a. The activation energies as estimated by regression are 0.42 eV for Na$_{2.875}$OCl and 0.47 eV for Na$_{2.75}$Ca$_{0.125}$OCl. The extrapolated conductivity at 300 K for Na$_{2.75}$Ca$_{0.125}$OCl is 0.53 − 4.41 µS/cm. The value is smaller than that of Na$_{2.875}$OCl, 3.92 − 8.19µS/cm. Here, the uncertainty on the conductivity reflects the uncertainty on E$_a$ as obtained by Bayesian inference under the prior that both log(σT) and E$_a$ are normally distributed [46]. The higher activation energy and hence, the smaller ionic conductivity for the doped case agrees with our previous NEB simulation results: the binding between the substitutional defect and the associated V$^{'}_{Na}$ leads to greater migration barrier.

We should note that only one V$^{'}_{Na}$ is considered in our AIMD simulations. However, the increase in V$^{'}_{Na}$ concentration because of the addition of M$^{\bullet}_{Na}$ may dominate over the adverse effects due to the binding between V$^{'}_{Na}$ and M$^{\bullet}_{Na}$. Such an increased defect concentration, in turn, leads to an overall enhancement of the ionic conductivity.
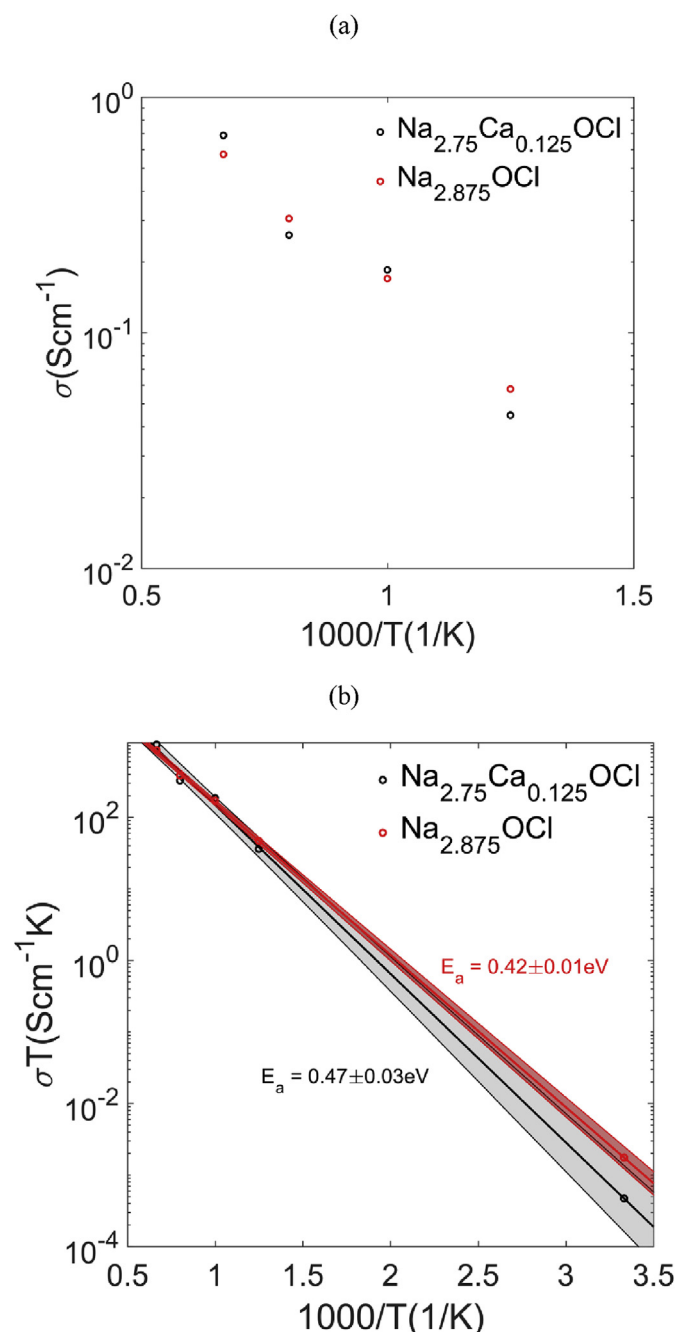
(a)

(b)

Fig. 8. The Arrhenius plot of conductivity against temperature for $Na_{2.875}OCl$ and $Na_{2.75}Ca_{0.125}OCl$. Panel (a), the conductivity at the four simulation temperatures. Panel (b), the linear regression and extrapolation of the temperature-normalized conductivity to low temperature. The shaded region denote 95% predictive interval.

Indeed, experimental literatures suggest the utilization of larger substitutional defects, such as $Sr^{\bullet}_{Na}$ and $Ba^{\bullet}_{Na}$, instead of the smaller ones [22,23]. Such choice is primarily motivated by the lower substitutional solution energies, as discussed in section 3.3, implying that it is easier to incorporate the larger substitutional defects and create $V^{'}_{Na}$ in the structure. Nonetheless, if the $M^{\bullet}_{Na} - V^{'}_{Na}$ binding effect is non-negligible, our simulations indicate that $Ca^{\bullet}_{Na}$ may be another potential candidate for substitution to Na_3OCl because of the relatively lower binding energies, and hence smaller impact to the Na diffusion.

4. Conclusion

We conducted first-principles DFT calculations to study the chemistry of defects, the impact of selected alkaline earth element substitutions, and the transportation of Na ion in Na_3OCl. Our results suggest that, in the pristine Na_3OCl antiperovskite, the formation of NaCl Schottky defect pairs is energetically more favorable than the other defect pairs studied. Consequently, it is likely that Na transport is enabled by a vacancy hopping mechanism, in analogy with Li_3OCl. The availability and impact of alkaline earth element substitution were assessed by calculating both substitutional and binding energies. Our results indicate that larger alkaline earth metals are more energetically favorable for substitution. However, they also lead to stronger $M^{\bullet}_{Na} - V^{'}_{Na}$ binding due to a more compact adjacent type configuration with smaller $M^{\bullet}_{Na} - V^{'}_{Na}$ distance. Based on these results, we conducted NEB and AIMD simulations. Both simulations indicate that the $M^{\bullet}_{Na}$ substitution leads to the increase in the activation energy of Na migration. Such adverse effect can be minimized by choosing $M^{\bullet}_{Na}$ that have the weakest binding with the associated $V^{'}_{Na}$. Having the lowest $M^{\bullet}_{Na} - V^{'}_{Na}$ binding energy among the elements studied, we suggest that $Ca^{\bullet}_{Na}$ may be a potential substitutional defect candidate to be introduced into Na_3OCl in order to increase the vacancy concentration and thereby improve the Na conductivity of this promising material.

Appendix A. Supplementary information

Supplementary information related to this article can be found at http://dx.doi.org/10.1016/j.jpowsour.2018.03.073.

References

[1] J.M. Tarascon, Is lithium the new gold? Nat. Chem. 2 (2010) 510–510.
[2] P. Barpanda, G. Oyama, S.-I. Nishimura, S.-C. Chung, A. Yamada, A 3.8-V Earth-abundant Sodium Battery Electrode, Nat. Commun. 5 (2014) 4358.
[3] S. Komaba, W. Murata, T. Ishikawa, N. Yabuuchi, T. Ozeki, T. Nakayama, A. Ogata, K. Gotoh, K. Fujiwara, Electrochemical Na insertion and solid electrolyte interphase for hard-carbon electrodes and application to Na-Ion batteries, Adv. Funct. Mater. 21 (2011) 3859–3867.
[4] K.B. Hueso, M. Armand, T. Rojo, High temperature sodium batteries: status, challenges and future trends, Energy Environ. Sci. 6 (2013) 734–749.
[5] D. Larcher, J.M. Tarascon, Towards greener and more sustainable batteries for electrical energy storage, Nat. Chem. 7 (2015) 19–29.
[6] J.M. Tarascon, M. Armand, Issues and challenges facing rechargeable lithium batteries, Nature 414 (2001) 359–367.
[7] M.M. Thackeray, C. Wolverton, E.D. Isaacs, Electrical energy storage for transportation-approaching the limits of, and going beyond, lithium-ion batteries, Energy Environ. Sci. 5 (2012) 7854–7863.
[8] B.L. Ellis, L.F. Nazar, Sodium and sodium-ion energy storage batteries, Curr. Opin. Solid State Mater. Sci. 16 (2012) 168–177.
[9] V. Palomares, P. Serras, I. Villaluenga, K.B. Hueso, J. Carretero-Gonzalez, T. Rojo, Na-ion batteries, recent advances and present challenges to become low cost energy storage systems, Energy Environ. Sci. 5 (2012) 5884–5901.
[10] N. Kamaya, K. Homma, Y. Yamakawa, M. Hirayama, R. Kanno, M. Yonemura, T. Kamiyama, Y. Kato, S. Hama, K. Kawamoto, A. Mitsui, A lithium superionic conductor, Nat. Mater. 10 (2011) 682–686.
[11] M.D. Slater, D. Kim, E. Lee, C.S. Johnson, Sodium-ion batteries, Adv. Funct. Mater. 23 (2013) 947–958.
[12] Z. Lu, F. Ciucci, Metal borohydrides as electrolytes for solid-state Li, Na, Mg, and Ca batteries: a first-principles study, Chem. Mater. 29 (2017) 9308–9319.
[13] M.S. Whittingham, R.A. Huggins, Measurement of sodium ion transport in beta

alumina using reversible solid electrodes, J. Chem. Phys. 54 (1971) 414–416.

[14] B. Dunn, H. Kamath, J.M. Tarascon, Electrical energy storage for the grid: a battery of choices, Science 334 (2011) 928–935.

[15] H. Pan, Y.S. Hu, L. Chen, Room-temperature stationary sodium-ion batteries for large-scale electric energy storage, Energy Environ. Sci. 6 (2013) 2338–2360.

[16] F. Lalère, J.B. Leriche, M. Courty, S. Boulineau, V. Viallet, C. Masquelier, V. Seznec, An all-solid state NASICON sodium battery operating at 200 °C, J. Power Sources 247 (2014) 975–980.

[17] S. Song, H.M. Duong, A.M. Korsunsky, N. Hu, L. Lu, A Na^+ superionic conductor for room-temperature sodium batteries, Sci. Rep. 6 (2016) 32330.

[18] M. Tatsumisago, A. Hayashi, Sulfide glass-ceramic electrolytes for all-solid-state lithium and sodium batteries, Int. J. Appl. Glass Sci. 5 (2014) 226–235.

[19] A. Hayashi, K. Noi, A. Sakuda, M. Tatsumisago, Superionic Glass-Ceramic Electrolytes for Room-Temperature Rechargeable Sodium Batteries, Nat. Commun. 3 (2012) 856.

[20] A. Hayashi, K. Noi, N. Tanibata, M. Nagao, M. Tatsumisago, High sodium ion conductivity of glass–ceramic electrolytes with cubic Na_3PS_4, J. Power Sources 258 (2014) 420–423.

[21] Y. Zhao, L.L. Daemen, Superionic conductivity in lithium-rich anti-perovskites, J. Am. Chem. Soc. 134 (2012) 15042–15047.

[22] Y. Wang, Q. Wang, Z. Liu, Z. Zhou, S. Li, J. Zhu, R. Zou, Y. Wang, J. Lin, Y. Zhao, Structural manipulation approaches towards enhanced sodium ionic conductivity in Na-rich antiperovskites, J. Power Sources 293 (2015) 735–740.

[23] M.H. Braga, A.J. Murchison, J.A. Ferreira, P. Singh, J.B. Goodenough, Glass-amorphous alkali-ion solid electrolytes and their performance in symmetrical cells, Energy Environ. Sci. 9 (2016) 948–954.

[24] M.H. Braga, J.A. Ferreira, V. Stockhausen, J.E. Oliveira, A. El-Azab, Novel Li_3ClO based glasses with superionic properties for lithium batteries, J. Mater. Chem. A 2 (2014) 5470–5480.

[25] M.H. Braga, J.A. Ferreira, A.J. Murchison, J.B. Goodenough, Electric dipoles and ionic conductivity in a Na^+ glass electrolyte, J. Electrochem. Soc. 164 (2017) A207–A213.

[26] H. Nguyen, S. Hy, E. Wu, Z. Deng, M. Samiee, T. Yersak, J. Luo, S.P. Ong, Y.S. Meng, Experimental and computational evaluation of a sodium-rich anti-perovskite for solid state electrolytes, J. Electrochem. Soc. 163 (2016) A2165–A2171.

[27] J. Zhu, Y. Wang, S. Li, J.W. Howard, J. Neuefeind, Y. Ren, H. Wang, C. Liang, W. Yang, R. Zou, C. Jin, Y. Zhao, Sodium ion transport mechanisms in anti-perovskite electrolytes Na_3OBr and Na_4OI_2: an in situ neutron diffraction study, Inorg. Chem. 55 (2016) 5993–5998.

[28] Z. Lu, C. Chen, Z.M. Baiyee, X. Chen, C. Niu, F. Ciucci, Defect chemistry and lithium transport in Li_3OCl anti-perovskite superionic conductors, Phys. Chem. Chem. Phys. 17 (2015) 32547–32555.

[29] G. Kresse, J. Furthmüller, Efficient iterative schemes for *ab initio* total-energy

calculations using a plane-wave basis set, Phys. Rev. B 54 (1996) 11169–11186.

[30] J.P. Perdew, K. Burke, M. Ernzerhof, Generalized gradient approximation made simple, Phys. Rev. Lett. 77 (1996) 3865–3868.

[31] H.J. Monkhorst, J.D. Pack, Special points for Brillouin-zone integrations, Phys. Rev. B 13 (1976) 5188–5192.

[32] D.J. Evans, B.L. Holian, The nose–hoover thermostat, J. Chem. Phys. 83 (1985) 4069–4074.

[33] Z. Lu, F. Ciucci, Structural origin of the superionic Na conduction in $Na_2B_{10}H_{10}$ closo-borates and enhanced conductivity by Na deficiency for high performance solid electrolytes, J. Mater. Chem. A 4 (2016) 17740–17748.

[34] Y. Mo, S.P. Ong, G. Ceder, First principles study of the $Li_{10}GeP_2S_{12}$ lithium super ionic conductor material, Chem. Mater. 24 (2012) 15–17.

[35] K. Hippler, S. Sitta, P. Vogt, H. Sabrowsky, Structure of Na_3OCl, Acta Crystallogr. Sect. C Cryst. Struct. Commun. 46 (1990) 736–738.

[36] J. Ramanna, N. Yedukondalu, K. Ramesh Babu, G. Vaitheeswaran, *Ab initio* study of electronic structure, elastic and optical properties of anti-perovskite type alkali metal oxyhalides, Solid State Sci. 20 (2013) 120–126.

[37] A.D. Becke, K.E. Edgecombe, A simple measure of electron localization in atomic and molecular systems, J. Chem. Phys. 92 (1990) 5397–5403.

[38] Y. Zhang, Y. Zhao, C. Chen, *Ab initio* study of the stabilities of and mechanism of superionic transport in lithium-rich antiperovskites, Phys. Rev. B 87 (2013) 134303.

[39] H. Tang, Z. Deng, Z. Lin, Z. Wang, I.-H. Chu, C. Chen, Z. Zhu, C. Zheng, S.P. Ong, Probing solid–solid interfacial reactions in all-solid-state sodium-ion batteries with first-principles calculations, Chem. Mater. 30 (2018) 163–173.

[40] A. Emly, E. Kioupakis, A. Van der Ven, Phase stability and transport mechanisms in antiperovskite Li_3OCl and Li_3OBr superionic conductors, Chem. Mater. 25 (2013) 4663–4670.

[41] R. Mouta, M.Á.B. Melo, E.M. Diniz, C.W.A. Paschoal, Concentration of charge carriers, migration, and stability in Li_3OCl solid electrolytes, Chem. Mater. 26 (2014) 7137–7144.

[42] P.G. Sundell, M.E. Björketun, G. Wahnström, Thermodynamics of doping and vacancy formation in $BaZrO_3$ perovskite oxide from density functional calculations, Phys. Rev. B 73 (2006) 104112.

[43] J. Cheng, A. Navrotsky, Energetics of magnesium, strontium, and barium doped lanthanum gallate perovskites, J. Solid State Chem. 177 (2004) 126–133.

[44] M. Nakayama, M. Martin, First-principles study on defect chemistry and migration of oxide ions in ceria doped with rare-earth cations, Phys. Chem. Chem. Phys. 11 (2009) 3241–3249.

[45] R.F.W. Bader, Atoms in Molecules, John Wiley & Sons, Ltd, 2002.

[46] A. Gelman, J.B. Carlin, H.S. Stern, D.B. Dunson, A. Vehtari, D.B. Rubin, Bayesian Data Analysis, third ed., Taylor & Francis, 2013.